Green Chemistry

PAPER

View Article Online
View Journal | View Issue

Cite this: *Green Chem.*, 2021, **23**, 1220

Efficient electrochemical synthesis of a manganese-based metal–organic framework for H_2 and CO_2 uptake†

Aisha Asghar, [a] Naseem Iqbal, *[a] Tayyaba Noor,[b] Benson M. Kariuki, [c]
Luke Kidwell[c] and Timothy L. Easun *[c]

Received 29th September 2020,
Accepted 15th January 2021

DOI: 10.1039/d0gc03292a

rsc.li/greenchem

In this study Mn–DABDC (DABDC = diaminobenzenedicarboxylate, or 2,5-diaminoterephthalate) MOF was synthesised both *via* an electrochemical method, to make Mn–DABDC(ES), and *via* a conventional solvothermal approach, to make Mn–DABDC(ST). A Mn–BDC (BDC = benzenedicarboxylate) MOF was also prepared by a conventional solvothermal method for gas uptake capacity comparison. Investigation of the electrochemical synthesis parameters demonstrated that current density, electrolyte amount and reaction time were the most significant factors affecting crystal synthesis and product yield. The best conditions found for obtaining a crystalline MOF with high yield (93%) were 70 mA current, electrolyte 2.7 mmol/30 ml DMF and 2 h of reaction time. These optimized electrochemical conditions allow for a relatively fast MOF synthesis, important for reducing synthesis cost compared with conventional hydrothermal and solvothermal methods. The Mn–DABDC(ES) MOF sample was fully characterized to analyse its structure, thermal stability and surface area. The electrochemically synthesized MOF has high carbon dioxide uptake (92.4 wt% at 15 bar and 273 K) and hydrogen uptake (12.3 wt% at 80 bar and 77 K). This is the first amine-based manganese MOF synthesized electrochemically, and the method has excellent potential for reducing large-scale MOF production costs.

Introduction

Coordination chemistry has evolved as a most promising route to porous materials with precisely decorated interiors to obtain specific properties for versatile applications.[1] One of the most highly studied applications of metal–organic frameworks (MOFs) is the capture of CO_2 to address global energy and environmental issues.[2,3] Metal–organic frameworks have metal coordination sites bridged by organic ligands in highly ordered networks that often afford well defined structures, high crystallinity and large surface areas that can be used in catalysis, or gas separation applications.[4,5] Over the last two decades developments in MOF synthesis have enabled MOFs to become promising candidates for carbon dioxide capture, however there is often poor carbon dioxide gas selectivity from flue gas streams.[2,6] A notable development is in the functionalization of MOF structures, including selective functional group insertion within any given framework to serve specific end functions and impart desirable properties to the MOF materials.[2,7,8] Amine sites in particular show great affinity towards carbon dioxide and are known to be highly effective for CO_2 adsorption while also being amenable to use under dry or humid conditions.[7] We have recently reported the modification of a copper-based MOF during synthesis by doping with hexamethylenetetramine, resulting in the enhancement of carbon dioxide sorption over the unmodified framework.[9] In another study we reported that amine post synthetic modification on a Mn–DOBDC framework (DOBDC = 2,5-dihydroxyterepthalate) enhances water stability and carbon dioxide uptake of the MOF.[10]

A major challenge in preparing MOFs for CO_2 capture applications is still the energy intensive, tedious and laborious conventional solvothermal process for MOF synthesis. Electrochemical synthesis of MOFs was first reported by BASF in 2005, using anodic dissolution to synthesise the copper-based framework HKUST-1.[11,12] Most subsequent examples using this method have focussed on Cu and Zn frameworks, although examples exploiting Al and Fe have been

---

[a] *U.S.-Pakistan Centre for Advanced Studies in Energy (USPCAS-E), National University of Sciences & Technology (NUST), H-12, Islamabad, 44000, Pakistan. E-mail: naseem@uspcase.nust.edu.pk*

[b] *School of Chemical & Materials Engineering (SCME), National University of Sciences & Technology (NUST), H-12, Islamabad, 44000, Pakistan*

[c] *School of Chemistry, Cardiff University, Main Building, Park Place, Cardiff, CF10 3AT, UK. E-mail: EasunTL@cardiff.ac.uk*

† Electronic supplementary information (ESI) available. CCDC 1948926 and 2027762. For ESI and crystallographic data in CIF or other electronic format see DOI: 10.1039/d0gc03292a

reported.[13–17] Recent reports include Pirzadeh and co-workers, who electrochemically synthesized a $Cu_3(BTC)_2$ metal–organic framework for CO_2 and CH_4 separation,[18] and, in a hybrid approach, Mitra *et al.* grew Cu-based MOFs onto modified thin-film electrodes to study their electrochemical properties.[19] The electrochemical MOF synthesis process has advantages over conventional MOF syntheses including the potential for shorter reaction times and lower energy consumption with a relatively simple equipment setup.[18] Perhaps the most attractive feature of electrochemical synthesis is the mild reaction conditions, since these reactions can be performed at ambient pressure and temperature. Despite these advantages, it is still an under-exploited approach, especially in the synthesis of functionalised framework materials.[20] This study demonstrates the synthesis of a new amine-functionalised Mn–DABDC MOF using electrochemical synthesis to cut synthesis costs, important for future scale-up. The prepared material was fully characterized to analyse its structure, thermal stability and surface area. For comparison, a Mn–BDC MOF that lacks amine functionalisation was also synthesized using a traditional solvothermal method to compare CO_2 and H_2 adsorption of these MOFs.

Experimental

Materials

All the chemicals were purchased from Merck Sigma Aldrich and used as received.

Synthesis of $\{Mn_2(BDC)_2(DMF)_2\}_\infty$ (Mn–BDC)

Mn–BDC MOF was prepared using a conventional solvothermal method reported by Huiping *et al.* in 2016, with slight modifications.[21] Equimolar quantities (1 : 1) of Mn $(NO_3)_2·6H_2O$ (287 mg, 1 mmol) and terephthalic acid (160 mg, 1 mmol) were dissolved in 10 ml DMF in a 50 ml beaker. The contents were ultra-sonicated at 45 °C for 2 hours then the solution was transferred to 23 ml Teflon vials. These were each sealed in a Parr autoclave and heated in an oven at 110 °C for 24 hours to yield white crystalline material. Crystals obtained were washed thrice with DMF then thrice with THF (5 ml for each wash). The resulting crystals were dried overnight at room temperature to get 83% yield (371 mg). The sample was activated in vacuum oven at 130 °C for 12 hours before further analysis.

Electrochemical synthesis of $\{Mn_3(DABDC)_3(DMF)_4\}_\infty$ (Mn–DABDC(ES))

For electrochemical synthesis of Mn–DABDC, 2,5-diaminoterephthalic acid (588 mg, 3 mmol) was dissolved in 30 ml DMF. In another beaker, $NaNO_3$ (225 mg, 2.7 mmol) was mixed with 10 ml distilled water to serve as a conductive electrolyte for the reaction. These mixtures were combined and ultrasonicated for 1 hour at room temperature to ensure complete mixing of contents. Mn strips were prepared for reaction (10 cm long × 2 cm wide × 0.4 cm thick). Polishing was done with sandpaper (400 grit) to remove any oxide layer and washing with distilled water followed by ethanol.

The electrochemical synthesis reaction was performed by dipping these Mn strips (3 cm depth) in the reaction mixture keeping them 2 cm apart. A direct current (DC) supply was then attached to the electrodes and the current adjusted to 70 mA. As the reaction proceeded, light brown crystals were observed in the solution. The reaction was performed at ambient temperature and pressure (*i.e.* 20–22 °C and 1 atm). After 2 h, the product was collected, filtered and washed with DMF three times and then three times with THF (5 ml for each wash). The product obtained was dried at 60 °C in the oven for 4 hours to obtain 93% yield (1.29 g). The sample was activated in a vacuum oven at 130 °C for 12 hours before further analysis. This electrochemically synthesised material is named Mn–DABDC(ES) throughout the manuscript. Note: a series of reactions were performed to optimize time of reaction, current density and electrolyte concentration to obtain the best Mn–DABDC(ES) MOF yield; details of this series are in the ESI and Fig. S1.†

Solvothermal synthesis of $\{Mn_3(DABDC)_3(DMF)_4\}_\infty$ (Mn–DABDC(ST))

Samples of the Mn–DABDC framework were also prepared using the conventional solvothermal method to compare synthetic outcomes with the product obtained by electrochemical synthesis. Equimolar quantities (1 : 1) of Mn $(NO_3)_2·6H_2O$ (287 mg, 1 mmol) and 2,5-diaminoterephthalic acid (196 mg, 1 mmol) were dissolved in 10 ml DMF. After ultra-sonication at 45 °C for 2 hours the solution was transferred to 23 ml Teflon vials and sealed in a Parr autoclave and heated in an oven at 120 °C for 22 hours to yield light brown crystals. Crystals obtained were washed thrice with DMF then thrice with THF (5 ml for each wash). The resulting crystals were dried overnight at room temperature to obtain 78% yield (377 mg). The sample was activated in vacuum oven at 130 °C for 12 hours before further analysis. This solvothermally synthesised material is named Mn–DABDC(ST) throughout the manuscript.

Equipment and characterization

Electrochemical syntheses were performed under constant current or voltage using a RIGOL DC Power supply and RIGOL millimeter DM3058E. Single crystal X-ray diffraction data for Mn–DABDC and Mn–BDC MOFs were collected on an Agilent SuperNova Dual Atlas diffractometer with Mo and Cu sources and a CCD detector. Data reduction and integration was performed using CrysAlisPro. Powder X-ray diffraction (PXRD) patterns were collected on an X'PertPro Panalytical Chiller 59 diffractometer using copper Kα (1.5406 Å) radiation. A 2θ range from 5 to 40 degrees was used to record the diffraction pattern. A SHIMADZU IR Affinitt-1S spectrometer was used to obtain IR spectra. Thermogravimetic analyses (TGA) were performed using a PerkinElmer Pyris 1 TGA equipment. The temperature was increased from 25 °C to 700 °C at a heating rate of 5 °C min^{-1} under a flow of air (20 ml min^{-1}). Elemental analyses were performed using a FlashSmart NC ORG elemental analyser.

CO_2 adsorption experiments were performed on a Quantachrome Isorb-HP100 volumetric type sorption analyser. Samples were degassed at 130 °C under vacuum for 12 hours and then backfilled with helium gas prior to gas sorption studies. CO_2 sorption studies were performed at two selected temperatures, 273 K and 298 K, over a pressure range of 0.5–15 bar. H_2 adsorption studies were performed at 273 K and 77 K, over a pressure range of 0.5–80 bar. N_2 adsorption studies of prepared samples were conducted to analyse surface area and pore volume using a Quantachrome Nova 2200e at 77 K at a relative pressure of P/P_0 = 0.05–1.0.

Results and discussion

There are several known structures containing Mn(II) nodes and the BDC linker, the earliest being MOF-73,[21–23] but these were made using, and consist of, different metal : linker ratios and solvents to our material; herein we have formed a new Mn–BDC framework. Briefly, our Mn–BDC framework crystallises in a monoclinic geometry with a = 13.4484(4) Å, b = 10.1799(3) Å and c = 17.6560(5) Å, and α = 90°, β = 90.271(3)°, γ = 90°. Mn–BDC is composed of a ratio of 2 : 2 : 2 Mn : BDC : DMF and has broadly octahedral coordination at each Mn to one oxygen from a DMF molecule and five oxygens from the carboxylates of the surrounding BDC linkers, which bridge Mn atoms to form chains down the a-axis. By comparison, Mn–DABDC(ES) has a ratio of 3 : 3 : 4 Mn : DABDC : DMF, and crystallizes in monoclinic geometry with a = 13.2985(7) Å, b = 10.0194(7) Å and c = 16.6456(7) Å, and α = 90°, β = 106.404(5)°, γ = 90°. The Mn atoms form linear Mn_3 clusters in which each Mn atom is coordinated by six oxygen atoms in a distorted octahedral arrangement; the two outer Mn atoms are each capped by two DMF molecules and coordinated by three carboxylate groups, with the carboxylates bridging the outer Mn atoms to the central Mn atom. These clusters are bridged by DABDC linkers in layers, with the layers separated by interdigitated cluster-capping DMF molecules. Further details are given in Table S2† and the structures for Mn–BDC and Mn–DABDC(ES) are shown in Fig. 1 & 2 respectively.

FTIR spectra of the prepared materials confirmed the presence of representative functional groups indicative of Mn–BDC and Mn–DABDC MOF formation (Fig. S2†). Sharp peaks representative of symmetric and asymmetric stretching of carboxylates bonded to Mn are observed at 1535 cm^{-1} and 1367 cm^{-1} in the Mn–DABDC sample.[3] Both samples contain a broad band at around 3250 cm^{-1}, which can be attributed to O–H stretching vibrations of adsorbed atmospheric water.[24,25] In addition to the C–H stretches in both samples around

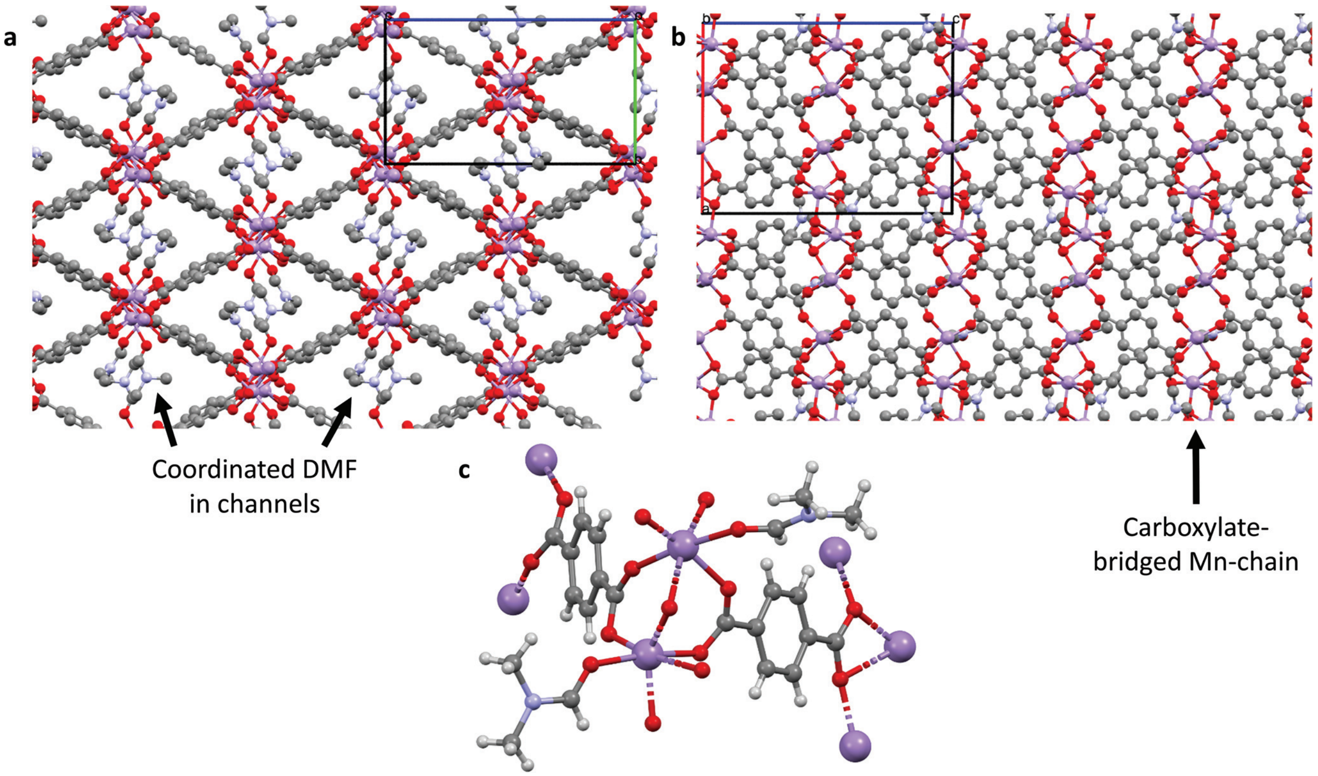

Fig. 1 Crystal structure of Mn–BDC. (a) Packing diagram down the a-axis showing coordinated solvent-filled channels; (b) packing diagram down the b-axis showing carboxylate-bridging of Mn(II) chain; (c) metal coordination diagram showing the Mn(II) and ligand coordination environments. Purple atoms represent Mn, red are oxygen, grey are carbon, blue are nitrogen and white are hydrogen atoms (omitted in (a) and (b) for clarity).

3000 cm^{-1}, Mn–DABDC also shows an N–H stretch at ~3650 cm^{-1}.

The PXRD patterns of the as-synthesized Mn–BDC, Mn–DABDC(ES), Mn–DABDC(ST), and those simulated from single crystal XRD are shown in Fig. 3 and 4. PXRD patterns indicate in all cases the formation of highly crystalline material. PXRD patterns for Mn–DABDC produced from solvothermal synthesis and electrochemical synthesis indicate the same framework is synthesized with both methods, and in almost all solid products produced during the electrochemical parameter optimisation the Mn–DABDC MOF phase was formed with no apparent secondary phases (see ESI and Fig. S2†). Exceptions to this were the presence of a peak at 25° 2*θ* indicating unreacted crystalline DABDC linker remaining when current density was too low for efficient conversion to product (Fig. S2 pattern S1†), and the presence of small additional peaks, most notably around 11–12° and 25–27° 2*θ*, in the sample with the lowest quantity of electrolyte (Fig. S2 pattern S4†). There is also good agreement between the simulated and as-synthesized (optimised synthesis) PXRD patterns, indicating that the single crystals studied are representative of the bulk samples, which in the optimised syntheses exhibit good phase purity and absence of manganese dioxide.[26] The optimised product yield of Mn–DABDC obtained by electrochemical synthesis for 2 hours at room temperature was 93%, compared with only 78% obtained from the 22 hours, 120 °C solvothermal method. This improvement is possibly as a result of electrochemical delivery of metal ions from the manganese electrode at a rate determined by the electrolysis, combined with ready provision of nitrate counterions from the excess present as part of the electrolyte. Indeed, the nitrate ions can be recycled during the synthesis rather than having to be supplied stoichiometrically as part of the $Mn(NO_3)_2$ salt used in the solvothermal synthesis. These differences evidently have a marked impact on the reaction kinetics and hence may affect the resulting crystal size and defect content. The SEM images of Mn–BDC and Mn–DABDC are therefore presented in Fig. S5.† SEM results show a range of particle morphologies including flat hexagonal rods stacked on each other for Mn–DABDC(ES), a mixture of hexagonal rods and flake structures for Mn–DABDC(ST), and loose laminar rod-like structures for Mn–BDC. The surface roughness of Mn–DABDC(ST) visually appears greater than that of Mn–DABDC(ES). The electrochemically-synthesised crystallites are quite clearly larger than those formed in both solvothermal syntheses, with the largest Mn–DABDC(ES) rod diameters reaching ~8 μm in contrast to 2–3 μm for Mn–DABDC(ST) and only 1–2 μm for Mn–BDC. Both changes in morphology and size of the electrochemically synthesised framework are consistent with a different crystal growth mechanism, a feature of interest for future study beyond the scope of this present work.

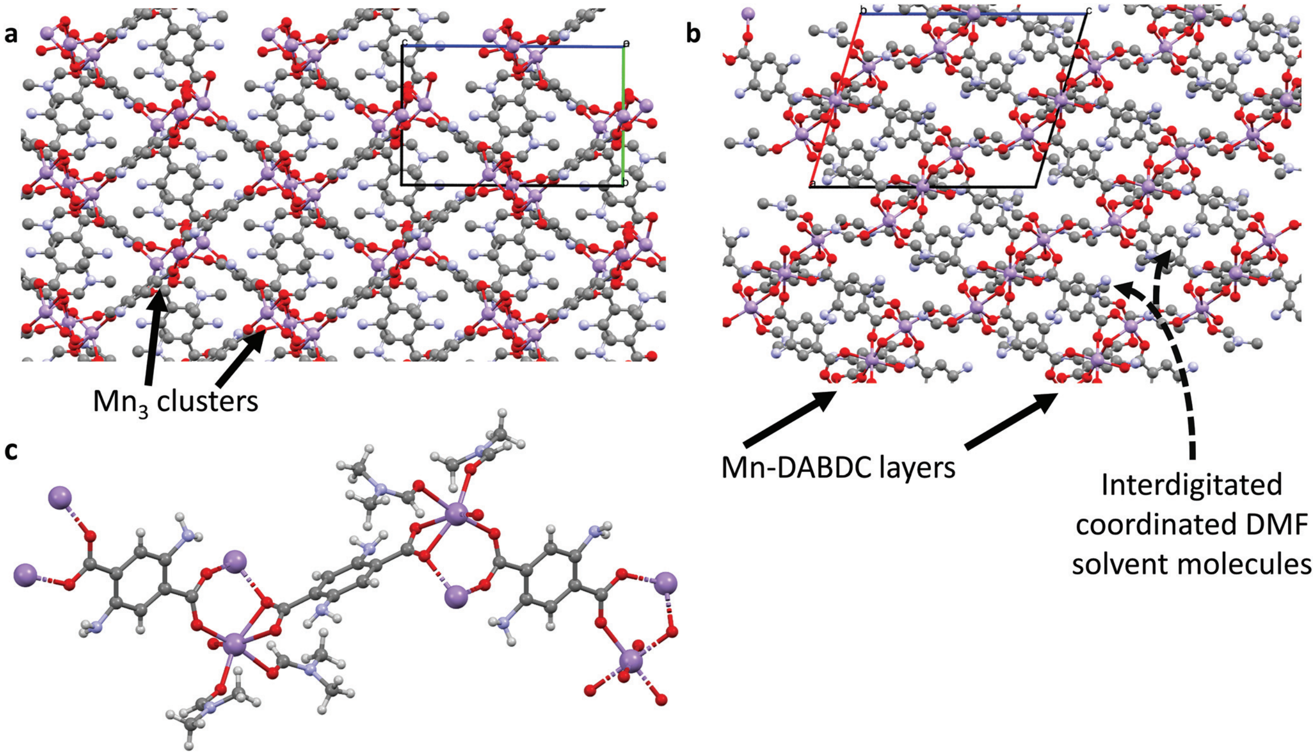

Fig. 2 Crystal structure of Mn–DABDC(ES). (a) Packing diagram down the *a*-axis showing Mn_3 cluster arrangement; (b) packing diagram down the *b*-axis showing layered structure with interdigitating DMF solvent molecules; (c) metal coordination diagram showing the Mn(II) and ligand coordination environments. Purple atoms represent Mn, red are oxygen, gray are carbon, blue are nitrogen and white are hydrogen atoms (omitted in (a) and (b) for clarity).

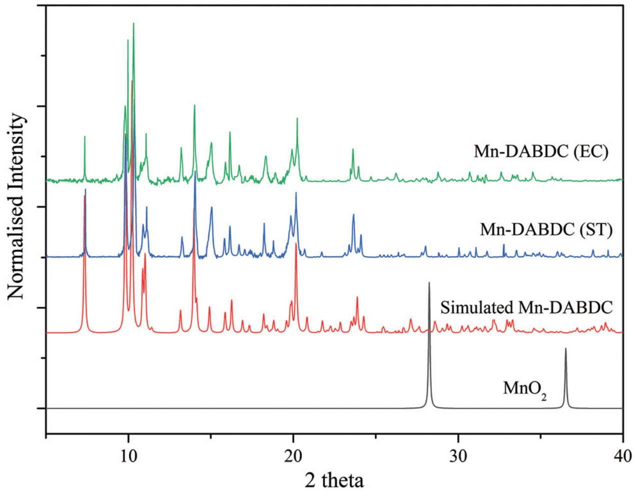

Fig. 3 Experimental PXRD patterns for Mn–DABDC(ES) synthesised electrochemically (green) and Mn–DABDC(ST) synthesised solvothermally (blue). Simulated PXRD pattern for Mn–DABDC (red) and PXRD pattern for MnO_2 (black). Patterns are offset on the vertical axis for clarity.

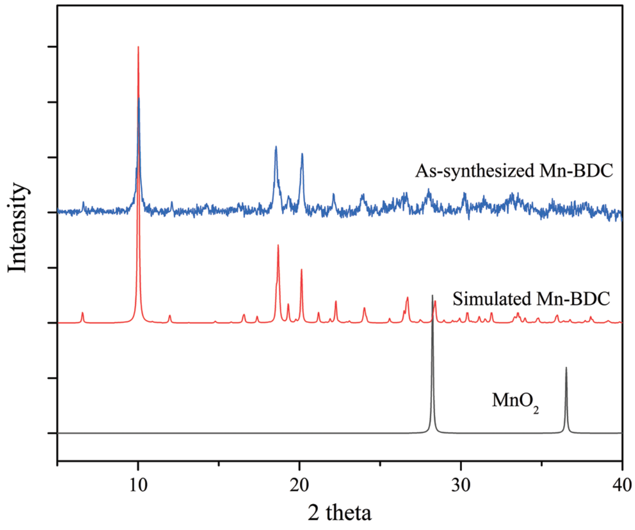

Fig. 4 Experimental (blue) and simulated (red) PXRD patterns for Mn–BDC, and PXRD pattern for MnO_2 (black).

Thermogravimetric analysis (TGA) was performed on Mn–BDC and Mn–DABDC (Fig. S4†). Some weight loss was observed below 100 °C for both MOFs indicating there was little surface adsorbed moisture.[27–29] There is a weight loss step between approx. 125–245 °C for both MOFs which we ascribe to the loss of coordinated DMF from the MOF structures.[6,30] There is prominent two-step DABDC linker degradation in the Mn–DABDC sample as the temperature increases above approximately 325 °C. No further weight losses were observed for Mn–DABDC above 560 °C, indicating residual metal oxide, while Mn–BDC MOF decomposed completely to the oxide at 425 °C, a notably lower temperature than Mn–DABDC.

CO_2 and H_2 adsorption capacities of Mn–BDC, Mn–DABDC (ES) and Mn–DABDC(ST)

The CO_2 adsorption capacity for both MOF materials was evaluated by monitoring pseudo equilibrium adsorption uptakes. Samples were first degassed at 130 °C for 12 hours. 200 mg of each sample was used for three consecutive adsorption–desorption cycles at 273 K and 298 K with adsorbate pressure ranging between 0.1 to 15 bar. The CO_2 capacities calculated at 273 K and 15 bar pressure were 11.5 mmol g^{-1} and 21 mmol g^{-1} for Mn–BDC and Mn–DABDC(ES), respectively. This trend also occurs for adsorption capacities recorded at 298 K (Fig. 5). Hydrogen uptake of Mn–DABDC(ES) MOF was 12.3 wt% at 80 bar pressure and 77 K (Fig. 6), and a pore size of 3.53 Å was calculated from gas sorption data. Moderate Q_{st} values were calculated for both gases in Mn–DABDC(ES) (Fig. S6†) which

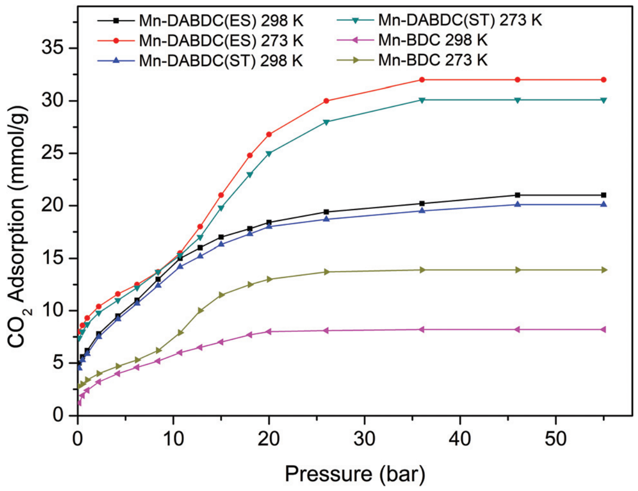

Fig. 5 CO_2 adsorption isotherms (mmol g^{-1}) for Mn–DABDC(ES), Mn–DABDC(ST) and Mn–BDC at 273 K and 298 K.

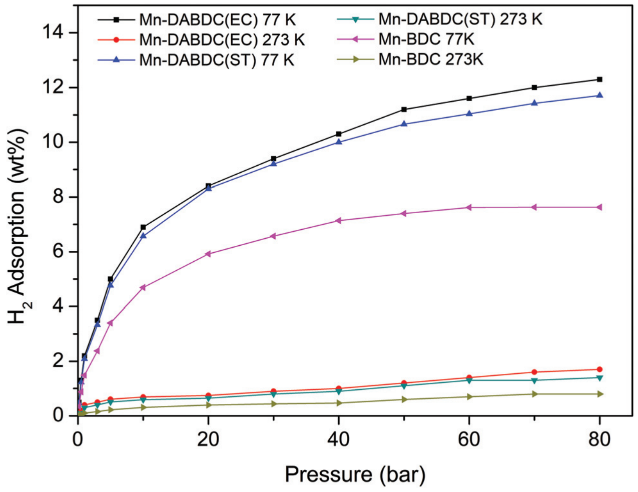

Fig. 6 H_2 adsorption isotherms for Mn–DABDC(ES), Mn–DABDC(ST) and Mn–BDC at 273 K and 77 K.

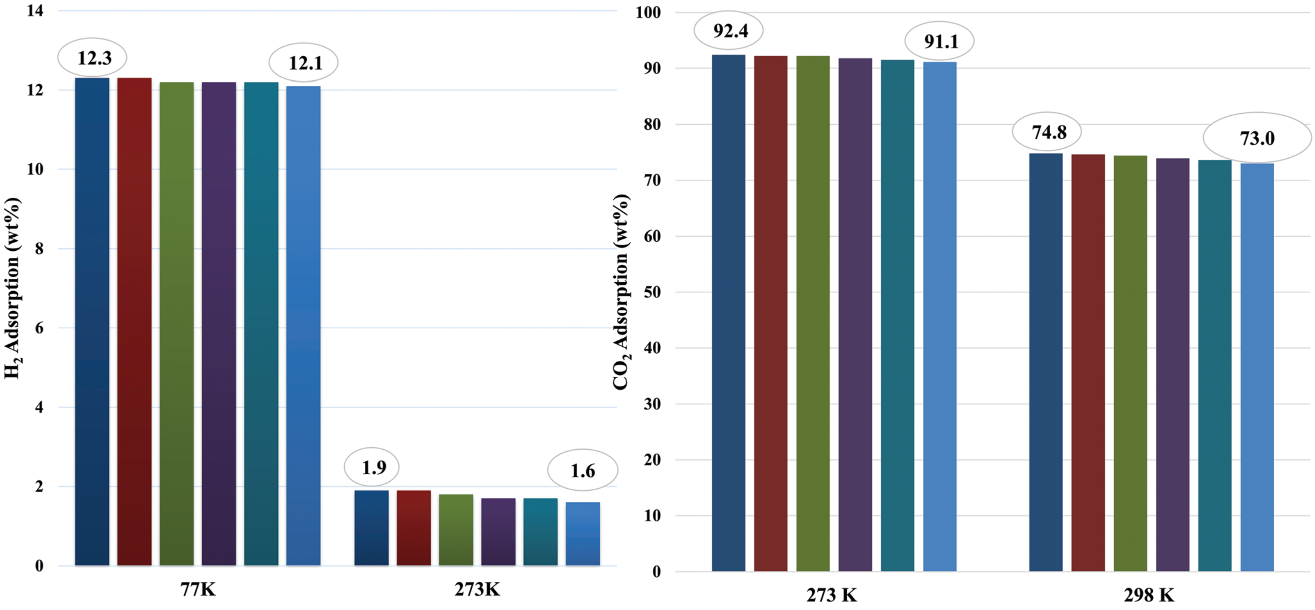

Fig. 7 H_2 and CO_2 adsorption at 15 bar by Mn–DABDC(ES) over six consecutive cycles.

Table 1 Surface area, CO_2 uptake and Q_{st} values for selected related and amine-containing MOFs

Material	BET surface area (m^2 g^{-1})	Temperature (K)	Pressure (bar)	CO_2 adsorption (wt%)	Q_{st} (kJ mol^{-1})	Ref.
Cu–BDC	708	273	1	5.28	—	9
			14	17.4		
Cu–BDC ⊃ HMTA	590	273	1	21.2	29.8	9
			14	52.8		
Mn–DOBDC	1256	273	1	33.0	29.0	10
			15	57.3		
		298	1	26.4		
			15	44.5		
EDA–Mn–DOBDC	1203	273	1	40.9	32.0	10
			15	70.3		
		298	1	33.5		
			15	57.2		
Amino-Zr-MOF	1220	273	1	19.62	29.3	31
	1395	296		12.54		
$Zn_2(NH_2BDC)_2$ (dpNDI)	897	273	1	29.04	46.5	32
fcu-MOF	605.8	273	1	5.59	25.4	33
		298		4.10		
Mg–ABDC	63	273	1.3	6.18	—	34
Co–ABDC	71	273	1.3	4.97	—	34
Sr–ABDC	2.5	273	1.3	0.8	—	34
Amino MIL-101 (Al)	2100	298	29.6	62.0	—	15
UiO-66-NH_2-GO	868	273	1	3.9	—	35
$Zn_4O(NH_2\text{-}BDC)_2$	2446	77	1	—	—	36
UMCM-1-NH_2	3917	77	1	—	4.6	37
MIL-101-PEI (polyethylenimine)	608	298	0.15	4.2	—	38
IRMOF-74-III-NH_2	2720	298	1	10.4		39
MFM-188	2568	298	1	23.7	20.8	40
NOTT-125	2471	298	1	18.2	25.4	41
Mn–DABDC	1453	273	1	40.9	32	Present study
		273	15	92.4		
		298	1	27.3		
		298	15	74.8		
Mn–BDC	667	273	1	14.9	33.5	Present study
		273	15	50.6		
		298	1	10.5		
		298	15	30.8		

demonstrated excellent regenerability under moderate desorption conditions (degassing under vacuum for one hour), with only a small decline in CO_2 and H_2 adsorption capacity over six successive test cycles (Fig. 7).

A comparison can also be made against the solvothermally-synthesised Mn–DABDC(ST) material. The CO_2 uptake at 55 bar of Mn–DABDC(ES) is slightly higher at both temperatures than that of Mn–DABDC(ST) (an increase of 6.3% at 273 K and 4.5% at 298 K) and markedly higher than that of Mn–BDC (an increase of 130% at 273 K and 136% at 298 K). The H_2 uptake of Mn–DABDC(ES) is similarly slightly higher than that of Mn–DABDC(ST) (an increase of 5% at 77 K and 21% at 273 K) and again markedly higher than that of Mn–BDC (an increase of 61% at 77 K and 113% at 273 K).

To put this work in a broader context, Table 1 provides a comparison of amine-based metal–organic frameworks for uptake of carbon dioxide and hydrogen. In previous studies, we reported amine-modification of Cu–BDC, a copper-based MOF, by doping the synthesis with hexamethylenetetramine (HMTA).[9] Despite a reduction in BET surface area from 708 to 590 $m^2 g^{-1}$, this modification afforded a 3- and 4-fold increase in 273 K CO_2 uptake over the unmodified Cu–BDC framework, at 1 and 14 bar respectively. We have also reported a post-synthetic modification approach, attaching ethylenediamine (EDA) to Mn–DODC, a manganese-based framework.[10] In that study, modification only reduced the BET surface area a small amount, from 1256 to 1203 $m^2 g^{-1}$, but again increased the 273 K CO_2 uptake, albeit by a smaller multiplier (see Table 1). However, it is notable in the present study that the incorporation of two primary amine groups per linker in Mn–DABDC (ES) results not only in the largest BET surface area of all three studies, 1453 $m^2 g^{-1}$, but in the highest overall CO_2 uptake of our amine-containing frameworks. At 273 K the CO_2 uptake of Mn–DABDC(ES) at 1 bar is 40.9 wt% and at 15 bar it is 92.4 wt%. These values surpass those of many related small-pore frameworks reported in the literature; some examples are given in Table 1. Given that the Q_{st} values at zero loading for EDA-MnDOBDC and Mn–DABDC(ES) are, perhaps unsurprisingly, essentially the same (32 kJ mol^{-1}) and most likely result from CO_2 binding to the primary amines in both cases, the improved performance of Mn–DABDC(ES) at higher pressure may be attributable in part to the greater surface area, and in part to the greater density of amine sites in the framework.

Conclusions

Mn–DABDC(ES) was successfully produced in good yield using electrochemical synthesis. Synthesis conditions were optimized to get a maximum product yield of 93%. Here, manganese metal cations were produced *in situ* using Mn electrodes, eliminating the need for the MOF-precursor metal salt as required in conventional solvothermal and hydrothermal MOF production approaches, since the counter-ions are transiently provided by the electrolyte solution and hence can be continuously recycled in the synthesis. SEM results revealed well-formed flat hexagonal rod-like crystals for Mn–DABDC(EC), larger than the rods produced for Mn–DABDC(ST) and Mn–BDC. The three MOF materials were tested for carbon dioxide and hydrogen gas uptake. Mn–DABDC(ES) demonstrated high carbon dioxide (92.4 wt% at 15 bar pressure and 273 K) and hydrogen uptake (12.3 wt% at 80 bar pressure and 77 K), a little higher than the respective CO_2 and H_2 uptake of the solvothermally synthesised Mn–DABDC(ST) material, with both outperforming the related Mn–BDC framework. These results are ascribed to the incorporation of basic amine groups into the organic ligand within the framework significantly enhancing electrostatic interactions between the framework and the guests, increasing gas sorption. The electrochemical synthesis has the following specific advantages over the traditional solvothermal synthesis: (i) the use of ambient temperature instead of 120 °C, (ii) the use of ambient pressure instead of high-pressure autoclaves, (iii) the use of mild reaction conditions that recycle the nitrate counterions, and (iv) a vastly reduced reaction time compared to the conventional solvothermal synthesis method. These advantages demonstrate a method of design and synthesis of new materials with high carbon dioxide and hydrogen uptake with the potential for cost-effective large-scale production in the future.

CCDC 1948926† contains the supplementary crystallographic data for the Mn–DABDC MOF structure and CCDC 2027762† contains the supplementary crystallographic data for the Mn–BDC MOF structure.

Conflicts of interest

There are no conflicts to declare.

Acknowledgements

The authors are grateful to the United States Centre for Advanced Studies in Energy, Pakistan and Higher Education Commission, Pakistan for providing financial support. TLE gratefully acknowledges the Royal Society for the award of a University Research Fellowship (6866), and Cardiff University for funding.

References

1 T. L. Easun and A. C. Nevin, *SPR Organomet. Chem.*, 2018, **42**, 54–79.
2 G. Férey, *Chem. Soc. Rev.*, 2008, **37**, 191–214.
3 O. K. Farha and J. T. Hupp, *Acc. Chem. Res.*, 2010, **43**, 1166–1175.
4 J. Lee, O. K. Farha, J. Roberts, K. A. Scheidt, S. T. Nguyen and J. T. Hupp, *Chem. Soc. Rev.*, 2009, **38**, 1450–1459.
5 *Functional Metal-Organic Frameworks: Gas Storage, Separation and Catalysis*, ed. M. Schröder, Springer Berlin Heidelberg, Berlin, Heidelberg, 2010, vol. 293.

6 J. R. Li, R. J. Kuppler and H. C. Zhou, *Chem. Soc. Rev.*, 2009, **38**, 1477–1504.

7 G. T. Rochelle, *Science*, 2009, **325**, 1652–1654.

8 M. D. Allendorf and V. Stavila, *CrystEngComm*, 2015, **17**, 229–246.

9 A. Asghar, N. Iqbal, T. Noor, M. Ali and T. L. Easun, *Nanomaterials*, 2019, **9**, 1063.

10 A. Asghar, N. Iqbal, L. Aftab, T. Noor, B. M. Kariuki, L. Kidwell and T. L. Easun, *R. Soc. Open Sci.*, 2020, **7**, 191934.

11 U. Mueller, H. Puetter, M. Hesse and H. Wessel, 2005, WO 2005/049892.

12 U. Mueller, M. Schubert, F. Teich, H. Puetter, K. Schierle-Arndt and J. Pastré, *J. Mater. Chem.*, 2006, **16**, 626–636.

13 A. Martinez Joaristi, J. Juan-Alcañiz, P. Serra-Crespo, F. Kapteijn and J. Gascon, *Cryst. Growth Des.*, 2012, **12**, 3489–3498.

14 H. Al-Kutubi, J. Gascon, E. J. R. Sudhölter and L. Rassaei, *ChemElectroChem*, 2015, **2**, 462–474.

15 P. Serra-Crespo, E. V. Ramos-Fernandez, J. Gascon and F. Kapteijn, *Chem. Mater.*, 2011, **23**, 2565–2572.

16 X. Zhang, K. Wan, P. Subramanian, M. Xu, J. Luo and J. Fransaer, *J. Mater. Chem. A*, 2020, **8**, 7569–7587.

17 O. J. De Lima Neto, A. C. de O. Frós, B. S. Barros, A. F. De Farias Monteiro and J. Kulesza, *New J. Chem.*, 2019, **43**, 5518–5524.

18 K. Pirzadeh, A. A. Ghoreyshi, M. Rahimnejad and M. Mohammadi, *Korean J. Chem. Eng.*, 2018, **35**, 974–983.

19 T. Mitra, F. Moreau, A. Nevin, C. U. Perotto, A. Summerfield, E. S. Davies, E. A. Gibson, T. L. Easun and M. Schröder, *Chem. Sci.*, 2018, **9**, 6572–6579.

20 E. R. Engel, E. R. Engel and J. L. Scott, *Green Chem.*, 2020, **22**, 3693–3715.

21 H. Hu, X. Lou, C. Li, X. Hu, T. Li, Q. Chen, M. Shen and B. Hu, *New J. Chem.*, 2016, **40**, 9746–9752.

22 F. Luo, Y.-X. Che and J.-M. Zheng, *Inorg. Chem. Commun.*, 2008, **11**, 358–362.

23 N. L. Rosi, J. Kim, M. Eddaoudi, B. Chen, M. O'Keeffe and O. M. Yaghi, *J. Am. Chem. Soc.*, 2005, **127**, 1504–1518.

24 A. Bétard, D. Zacher and R. A. Fischer, *CrystEngComm*, 2010, **12**, 3768–3772.

25 A. C. C. Chang, S. S. C. Chuang, M. Gray and Y. Soong, *Energy Fuels*, 2003, **17**, 468–473.

26 F. Su, C. Lu, S. C. Kuo and W. Zeng, *Energy Fuels*, 2010, **24**, 1441–1448.

27 J. A. Mason, T. M. McDonald, T. H. Bae, J. E. Bachman, K. Sumida, J. J. Dutton, S. S. Kaye and J. R. Long, *J. Am. Chem. Soc.*, 2015, **137**, 4787–4803.

28 K. Sumida, D. L. Rogow, J. A. Mason, T. M. McDonald, E. D. Bloch, Z. R. Herm, T. H. Bae and J. R. Long, *Chem. Rev.*, 2012, **112**, 724–781.

29 J. Borycz, L. C. Lin, E. D. Bloch, J. Kim, A. L. Dzubak, R. Maurice, D. Semrouni, K. Lee, B. Smit and L. Gagliardi, *J. Phys. Chem. C*, 2014, **118**, 12230–12240.

30 Y. S. Bae and R. Q. Snurr, *Angew. Chem., Int. Ed.*, 2011, **50**, 11586–11596.

31 H. R. Abid, J. Shang, H.-M. Ang and S. Wang, *Int. J. Smart Nano Mater.*, 2013, **4**, 72–82.

32 S. S. Dhankhar, N. Sharma, S. Kumar, T. J. D. Kumar and C. M. Nagaraja, *Chem. – Eur. J.*, 2017, **23**, 16204–16212.

33 K. Jiang, L. Zhang, T. Xia, Y. Yang, B. Li, Y. Cui and G. Qian, *Sci. China Mater.*, 2019, **62**, 1315–1322.

34 Y. Yang, R. Lin, L. Ge, L. Hou, P. Bernhardt, T. E. Rufford, S. Wang, V. Rudolph, Y. Wang and Z. Zhu, *Dalton Trans.*, 2015, **44**, 8190–8197.

35 Y. Cao, H. Zhang, F. Song, T. Huang, J. Ji, Q. Zhong, W. Chu and Q. Xu, *Materials*, 2018, **11**, 589.

36 J. L. C. Rowsell and O. M. Yaghi, *J. Am. Chem. Soc.*, 2006, **128**, 1304–1315.

37 Z. Wang, K. K. Tanabe and S. M. Cohen, *Chem. – Eur. J.*, 2010, **16**, 212–217.

38 J. Zhu, L. Wu, Z. Bu, S. Jie and B. G. Li, *ACS Omega*, 2019, **4**, 3188–3197.

39 A. M. Fracaroli, H. Furukawa, M. Suzuki, M. Dodd, S. Okajima, F. Gándara, J. A. Reimer and O. M. Yaghi, *J. Am. Chem. Soc.*, 2014, **136**, 8863–8866.

40 F. Moreau, I. da Silva, N. H. Al Smail, T. L. Easun, M. Savage, H. G. W. Godfrey, S. F. Parker, P. Manuel, S. Yang and M. Schröder, *Nat. Commun.*, 2017, **8**, 14085.

41 N. H. Alsmail, M. Suyetin, Y. Yan, R. Cabot, C. P. Krap, J. Lü, T. L. Easun, E. Bichoutskaia, W. Lewis, A. J. Blake and M. Schröder, *Chem. – Eur. J.*, 2014, **20**(24), 7317–7324.